Thin–Walled Structures 231 (2026) 115414

Contents lists available at ScienceDirect

Thin-Walled Structures

journal homepage: www.elsevier.com/locate/tws

Full length article

Substructuring-based section characterization of thin-walled beams from shell finite element models

Claudio Caccia *, Marco Morandini, Pierangelo Masarati

Department of Aerospace Science and Technology, Politecnico di Milano, Milan, Italy

ARTICLE INFO

Keywords:
Thin-walled structures
Beam section characterization
Substructuring
Shell finite elements
Kirchhoff–Love shells
Reissner–Mindlin shells
Classical lamination theory
Stiffness coupling

ABSTRACT

Accurate beam sectional stiffness and inertia properties are essential for reliable one-dimensional modeling of thin-walled structures, particularly in the presence of material anisotropy and coupling effects. A recently proposed substructuring-based framework extracts these properties directly from a short three-dimensional finite element beam slice model by (i) statically condensing internal degrees of freedom, (ii) enforcing equilibrated generalized load states through reduced interface handles, and (iii) matching the slice strain and kinetic energies with those of an equivalent beam model. While the original formulation was designed for solid-element discretizations, many thin-walled structural components of practical use are more efficiently modeled with shell elements, whose nodal kinematics include rotational degrees of freedom. This paper extends the framework to Kirchhoff–Love and Reissner–Mindlin shell formulations by redefining the rigid interface-handle mapping to constrain both translational and rotational degrees of freedom consistently. The method is validated on: (i) a thin-walled circular cylinder with analytical reference properties; (ii) a flat plate over a range of thicknesses, from thin to moderately thick, to assess transverse shear effects; (iii) a steel I-section (IPE100), to evaluate shell versus three-dimensional accuracy and flange-web junction effects; and (iv) a laminated orthotropic rectangular box modeled using equivalent single-layer shells based on classical lamination theory, with comparisons against ply-resolved three-dimensional references. The study provides practical guidelines for choosing shell formulations and discretization requirements for extracting sectional properties in thin-walled applications.

1. Introduction

Beam models remain the workhorse for the analysis and design of slender and thin-walled components, providing efficient system-level simulations while retaining the dominant structural behavior. Their predictive capability depends critically on the quality of the sectional stiffness and inertia properties that link generalized internal resultants to generalized strains. For simple isotropic sections, classical formulas date back to de Saint-Venant and successors; however, modern thin-walled structures often exhibit complex geometries, heterogeneous and anisotropic materials, and pronounced coupling effects (e.g., bending-torsion, shear-torsion), making purely analytical characterization impractical. General numerical frameworks for anisotropic beam section characterization were established in seminal works and later refined, and comprehensive reviews are available in the literature [1,2].

A practical approach to obtain sectional properties consists of analyzing a short three-dimensional finite element (FE) slice and extracting equivalent one-dimensional stiffnesses from its response. Such slice-based approaches can be sensitive to boundary conditions and may struggle to represent the polynomial axial variation of beam kinematics when only two cross-sections are considered. To address these issues, a substructuring-based formulation was recently introduced to compute the full 6×6 sectional stiffness matrix and corresponding inertial quantities from a short FE subdomain, without requiring long specimens and while naturally accounting for warping and coupling effects [3].

In thin-walled applications, shell elements are often preferred over solids due to their favorable cost-to-accuracy ratio, especially when the thickness is small compared to other dimensions. However, shell FE nodes carry rotational degrees of freedom in addition to displacements, and their numerical behavior depends on the underlying shell kinematics (Kirchhoff–Love vs Reissner–Mindlin) and on practical discretization issues, such as locking and stabilization [4–6]. These aspects directly affect how rigid interface handles must be defined when the original substructuring-based extraction framework is applied to shells.

The approach presented in this work provides:

* Corresponding author.
E-mail address: claudiogiovanni.caccia@polimi.it (C. Caccia).

https://doi.org/10.1016/j.tws.2026.115414
Received 26 March 2026; Received in revised form 16 July 2026; Accepted 17 July 2026
Available online 23 July 2026

- an extension of the substructuring-based section characterization framework to shell FE discretizations by redefining the rigid interface-handle mapping to include nodal rotations;
- a validation campaign on canonical benchmarks (circular pipe and flat plate); quantifying convergence and the impact of shell kinematics on extracted stiffness terms, with emphasis on shear-related components;
- a steel I-section (IPE100) benchmark assessing shell versus three-dimensional accuracy and flange-web junction effects;
- an application to a laminated orthotropic thin-walled box using classical lamination theory (CLT)-based equivalent single-layer shell models, with comparison against detailed three-dimensional laminate references to assess typical error levels in practical composite structures;
- an application-oriented composite helicopter-blade section, based on a NACA 23012 shell skin with internal spar-strip reinforcements, demonstrating the use of the method on a realistic multi-component composite thin-walled section;

2. Background

The literature on thin-walled members combines: (i) classical thin-walled theories for idealized geometries, (ii) numerical cross-section analysis methods aimed at extracting effective beam properties, and (iii) modal frameworks, developed primarily for stability and vibration problems, that offer physically meaningful families of cross-sectional deformation modes.

2.1. Sectional constitutive behavior and numerical characterization

In the elastic regime, the generalized internal resultants (axial force, shear forces, torsional moment, bending moments) collected in $\mathbf{F}_{\text{gen}}$ are related to the generalized strains $\boldsymbol{\varepsilon}_{\text{gen}}$ through

$$\mathbf{F}_{\text{gen}} = \mathbf{D}\,\boldsymbol{\varepsilon}_{\text{gen}}, \tag{1}$$

where $\mathbf{D}$ is the 6×6 sectional stiffness matrix (possibly fully populated due to coupling).

2.2. Classical thin-walled response and coupling effects

Classical thin-walled results for torsion, shear flow, and warping (e.g., Saint-Venant torsion, Bredt-Batho for closed thin-walled cells, and Vlasov-type extensions) remain essential for interpreting the mechanics of open/closed sections and the origin of coupling effects. However, extending closed-form formulas to arbitrary multi-cell geometries, spatially varying thickness, cut-outs, and anisotropic laminates is non-trivial, and coupling terms may become essential in practical applications.

2.3. Numerical cross-section analysis for beam models

A broad class of numerical methods targets the computation of sectional stiffness and inertia properties by solving two-dimensional problems on the cross-section, identifying warping functions, and enforcing energetic equivalence. These approaches underpin geometrically exact beam formulations, including anisotropic extensions, and are well covered in foundational works and later reviews [1,2,7].

The substructuring-based framework employed here follows a complementary route: it extracts sectional properties directly from a short three-dimensional finite element slice through condensation and energetic equivalence, thereby leveraging standard FE discretizations while avoiding the need for long specimens and naturally accounting for warping and coupling effects [3].

2.4. Modal thin-walled frameworks: Generalized beam theory and finite strip methods

Generalized Beam Theory (GBT) provides a modal description of thin-walled cross-section deformation by constructing families of cross-sectional modes (e.g., global, distortional, local, shear-related) and tracking their axial evolution. This modal viewpoint is especially effective for buckling, post-buckling, and vibration analyses of prismatic thin-walled members, and has motivated extensive developments and applications in the thin-walled structures' literature (see, e.g., [8–11] and references therein).

Several computational tools implement GBT for practical analyses. In particular, *GBTUL* (“GBT at the University of Lisbon”) is a widely used freeware program that performs elastic buckling (bifurcation) and vibration analyses of prismatic thin-walled members within the GBT framework, providing visualization of cross-section deformation modes and their contribution to the computed response [12].

A complementary and very efficient route for elastic stability is offered by the finite strip method (FSM), widely used for prismatic thin-walled members (especially in cold-formed steel). Constrained FSM variants provide systematic mode identification (local/distortional/global) and the construction of signature curves. *CUFSM* is an open-source implementation of conventional and constrained FSM that has become a widely adopted tool in the field for elastic buckling mode analysis and classification in the thin-walled structures community [13].

While GBTUL and CUFSM primarily target stability and mode characterization, their popularity highlights the practical value of tools that bridge detailed thin-walled behavior with reduced descriptions.

The present work addresses a complementary need: extracting the full 6×6 sectional stiffness matrix and associated inertial terms to support general beam-level simulations (including coupled multiphysics), using standard FE discretizations (solids or shells) through a unified framework based on substructuring and energetic equivalence.

2.5. Shell kinematics: Kirchhoff–love vs Reissner–Mindlin

Kirchhoff–Love (KL) shell theory neglects transverse shear deformation and assumes that normals to the mid-surface remain straight and normal after deformation. It is well-suited for very thin structures but may become inaccurate when transverse shear contributes appreciably. Reissner–Mindlin (RM) shells retain transverse shear deformation through independent rotational degrees of freedom, at the cost of requiring additional transverse-shear constitutive information and, in practice, shear correction factors [6,14].

For sectional property extraction, the KL vs RM choice is expected to affect primarily terms influenced by transverse shear (shear stiffness and, depending on geometry, torsion and coupling terms), whereas membrane and bending-dominated stiffness components should be less sensitive in slender thin-walled regimes.

2.6. Practical aspects of shell finite elements

Shell elements are frequently formulated as “degenerated” isoparametric solids; thus, numerical accuracy may be limited by shear and membrane locking in the thin limit, or by spurious zero-energy (hourglass) modes in under-integrated formulations. Standard remedies include reduced/selective integration, mixed interpolation, assumed strain methods, and stabilization techniques [5,15,16].

These issues influence the robustness of extracted stiffness terms when very thin walls are modeled with low-order RM shells.

3. Method

This section summarizes the extraction procedure and highlights the modifications required for shell FE models. The core framework

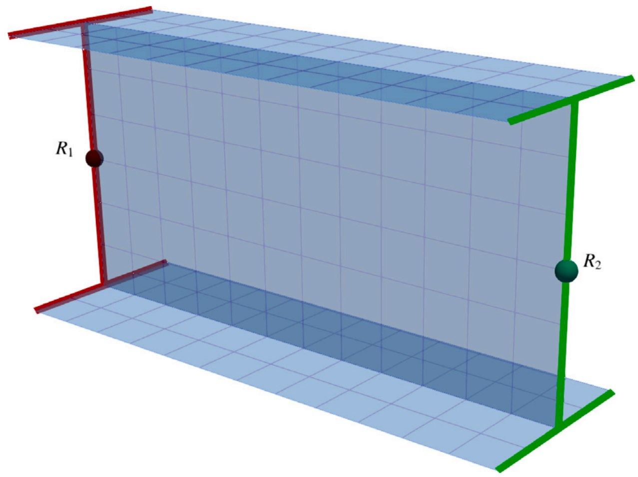

Fig. 1. Thin-walled beam slice: interface sections and handles R_1 and R_2 (highlighted in red and green).

is based on (i) static condensation to an interface problem, (ii) a reduced interface-handle representation, and (iii) energetic equivalence to identify sectional compliance and stiffness matrices. For full algebraic details of the slice formulation and assembly, the reader is referred to the original formulation [3].

3.1. Static condensation of a three-dimensional slice

Consider a linear elastic FE model of a short prismatic slice of length ℓ, with displacement vector $\mathbf{u}$, stiffness matrix $\mathbf{K}$, and (for inertia) mass matrix $\mathbf{M}$. Partition the degrees of freedom into interface (R) and internal (L) subsets, corresponding to the two end cross-sections and the interior:

$$\begin{bmatrix} \mathbf{K}_{RR} & \mathbf{K}_{LR}^T \\ \mathbf{K}_{LR} & \mathbf{K}_{LL} \end{bmatrix} \begin{Bmatrix} \mathbf{u}_R \\ \mathbf{u}_L \end{Bmatrix} = \begin{Bmatrix} \mathbf{f}_R \\ \mathbf{f}_L \end{Bmatrix}. \tag{2}$$

Assuming no external forces act on the internal DOFs ($\mathbf{f}_L = \mathbf{0}$), the internal DOFs are statically condensed, yielding a dense interface stiffness

$$\mathbf{K}_{BB} = \mathbf{K}_{RR} - \mathbf{K}_{LR}^T \mathbf{K}_{LL}^{-1} \mathbf{K}_{LR}. \tag{3}$$

A consistent condensed interface mass matrix $\mathbf{M}_{BB}$ can be obtained analogously and is used for inertial properties [17].

3.2. Reduced interface handles

The two interface portions at the ends of the slice are indexed by $i = 1, 2$, and their associated handles are shown in Fig. 1. A reduced six-dimensional "handle" $\mathbf{q}_{R_i} \in \mathbb{R}^6$ is associated with each interface portion, collecting three displacements and three infinitesimal (linearized) rotations about a reference point $\mathbf{p}_{i_0}$. The interface displacement vector is constrained as

$$\mathbf{u}_R = \mathbf{H}\,\mathbf{q}_R, \qquad \mathbf{q}_R = \begin{Bmatrix} \mathbf{q}_{R_1} \\ \vdots \\ \mathbf{q}_{R_k} \end{Bmatrix}. \tag{4}$$

This defines the rigid-body component of the interface motion associated with the handles.

Solid (displacement-only) interface nodes. If interface nodes carry displacements only (typical of solid-element discretizations), the node-level mapping block for node j on portion i is

$$\mathbf{H}_{i_j}^{(\mathrm{solid})} = \begin{bmatrix} \mathbf{I} & -\left(\mathbf{p}_{i_j} - \mathbf{p}_{i_0}\right)\times \end{bmatrix}, \qquad \mathbf{H}_{i_j}^{(\mathrm{solid})} \in \mathbb{R}^{3\times 6}. \tag{5}$$

Shell (displacement + rotation) interface nodes. For shell FE models, each shell interface node includes displacements and rotations, i.e. $\mathbf{u}_{i_j}^{(\mathrm{shell})} \in \mathbb{R}^6$. Assuming that nodal rotations, consistently with standard shell implementations, are expressed in a common (global) reference frame, a rigid-body-like constraint requires them to match the handle rotation, leading to the node-level mapping

$$\mathbf{H}_{i_j}^{(\mathrm{shell})} = \begin{bmatrix} \mathbf{I} & -\left(\mathbf{p}_{i_j} - \mathbf{p}_{i_0}\right)\times \\ \mathbf{0} & \mathbf{I} \end{bmatrix}, \qquad \mathbf{H}_{i_j}^{(\mathrm{shell})} \in \mathbb{R}^{6\times 6}. \tag{6}$$

The global $\mathbf{H}$ matrix in Eq. (4) is assembled by stacking node-level blocks and placing interface portions on the diagonal, analogously to the solid case.

The handle mapping does not imply that the interface section is forced to remain rigid in the finite element solution. Rather, it provides the rigid-body part of the retained interface kinematics, while the remaining interface degrees of freedom are used to describe warping of the section. For each interface portion, a complementary basis $\mathbf{C}_i$ is introduced such that

$$\begin{bmatrix} \mathbf{H}_i & \mathbf{C}_i \end{bmatrix} \tag{7}$$

spans the retained interface space. The columns of $\mathbf{C}_i$ are chosen orthogonal to the rigid-handle space,

$$\mathbf{C}_i^T \mathbf{H}_i = \mathbf{0}, \tag{8}$$

for instance by completing $\mathbf{H}_i$ through a QR factorization. The interface displacement can therefore be decomposed as

$$\mathbf{u}_{R_i} = \mathbf{H}_i \mathbf{q}_{R_i} + \mathbf{C}_i \mathbf{q}_{d_i}, \tag{9}$$

where $\mathbf{q}_{R_i}$ contains the six rigid-handle coordinates and $\mathbf{q}_{d_i}$ collects the generalized warping coordinates of the interface portion. In the shell case, both $\mathbf{H}_i$ and $\mathbf{C}_i$ are built in the space of shell nodal displacements and rotations, so that the complementary part can include warping contributions in both translational and rotational degrees of freedom.

3.3. Equilibrated generalized load states and compliance identification

Let the generalized internal resultants at a reference station be defined as

$$\mathbf{g}_{R_{\mathrm{ref}}} = \begin{Bmatrix} \mathbf{f} \\ \mathbf{m} \end{Bmatrix} \in \mathbb{R}^6, \tag{10}$$

with forces $\mathbf{f}$ and moments $\mathbf{m}$. In the absence of distributed loads, global equilibrium implies an affine axial variation of resultants along the slice,

$$\mathbf{g}_R(\xi) = \left(\mathbf{I} - (\xi - \xi_{\mathrm{ref}})\mathbf{T}\right) \mathbf{g}_{R_{\mathrm{ref}}}, \qquad \mathbf{T} = \begin{bmatrix} \mathbf{0} & \mathbf{0} \\ \mathbf{e}_1\times & \mathbf{0} \end{bmatrix}. \tag{11}$$

The FE slice problem is posed for multiple axial placements with respect to the same reference station, enforcing compatibility and the same equilibrated resultant set. In the following, $\mathbf{u}_R$ denotes the complete condensed interface displacement, including both the rigid-handle component and the complementary warping component introduced in Eq. (9). Solving the resulting overdetermined but consistent linear system in a least-squares sense yields a linear mapping between generalized resultants and condensed interface displacements,

$$\mathbf{u}_R = \mathbf{X}\,\mathbf{g}_{R_{\mathrm{ref}}}, \tag{12}$$

where $\mathbf{X}$ is obtained by applying unit generalized resultant load cases and collecting the corresponding interface responses [3].

The virtual strain work of the slice can then be written as

$$\delta\mathcal{W}_s = \delta\mathbf{g}_{R_{\mathrm{ref}}}^T \left(\mathbf{X}^T \mathbf{K}_{BB} \mathbf{X}\right) \mathbf{g}_{R_{\mathrm{ref}}}, \tag{13}$$

which defines the equivalent sectional compliance matrix

$$\mathbf{G} = \mathbf{X}^T \mathbf{K}_{BB} \mathbf{X}, \qquad \mathbf{D} = \mathbf{G}^{-1}. \tag{14}$$

Sectional inertial properties per unit span are obtained by matching the rigid-body kinetic energy of the condensed slice to that of a one-dimensional beam; compact closed-form expressions are provided in Appendix A.

Table 1
Geometry and material parameters for the circular cylinder benchmark.

Parameter	Symbol	Value	Units
Mean radius	R	0.5	m
Thickness	t	2	mm
Segment length	ℓ	1	m
Young's modulus	E	1	N/m^2
Poisson's ratio	ν	0.3	–
Density	ρ	1	kg/m^3

Table 2
Pipe benchmark: comparison between linear and quadratic shell discretizations for selected values of circumferential discretization N_θ.

N_θ	Element order	D_{11} (N)	D_{44} (N m^2)	D_{55} (N m^2)
18	linear	$6.251334 \cdot 10^{-3}$	$5.829823 \cdot 10^{-4}$	$7.657109 \cdot 10^{-4}$
	quadratic	$6.251334 \cdot 10^{-3}$	$5.830988 \cdot 10^{-4}$	$7.657094 \cdot 10^{-4}$
36	linear	$6.275213 \cdot 10^{-3}$	$5.988043 \cdot 10^{-4}$	$7.804318 \cdot 10^{-4}$
	quadratic	$6.275213 \cdot 10^{-3}$	$5.988396 \cdot 10^{-4}$	$7.804305 \cdot 10^{-4}$
54	linear	$6.279642 \cdot 10^{-3}$	$6.017721 \cdot 10^{-4}$	$7.831889 \cdot 10^{-4}$
	quadratic	$6.279642 \cdot 10^{-3}$	$6.017885 \cdot 10^{-4}$	$7.831870 \cdot 10^{-4}$
	analytical	$6.283185 \cdot 10^{-3}$	$6.041548 \cdot 10^{-4}$	$7.854013 \cdot 10^{-4}$

3.4. Axial discretization and slice length

The procedure enforces a beam-consistent axial variation of the generalized handle kinematics and allows a compatible axial variation of the complementary warping field. In the present formulation, the generalized handle kinematics are cubic in the axial coordinate. Consequently, a single axial layer of linear or quadratic elements cannot reproduce this variation exactly, and a minimum number of axial elements is required for the condensed slice response to approach the reference behavior. In our previous work on solid-element discretizations [3], satisfactory accuracy was typically achieved with about five quadratic elements along the axis, or approximately 10–15 linear elements, and the same guideline was adopted here for shell models. This requirement reflects a kinematic interpolation constraint rather than the need to capture end effects, since the slice is assumed to represent a region far from beam extremities. Numerical observations indicate that axial discretization primarily influences shear-related stiffness terms, whereas axial, bending, and torsional terms are largely insensitive. Accordingly, when shear stiffness is of interest, the axial mesh should be selected conservatively, and a brief sensitivity check is recommended when highly elongated elements are used. Because the substructuring step eliminates all internal degrees of freedom and retains only interface variables, increasing the number of axial layers beyond the stabilization threshold has no impact on the size or formulation/implementation of the reduced problem, only affecting the cost of the substructuring step.

4. Validation

For the canonical tube and plate benchmarks, unit values of the elastic modulus and density are used as normalized material parameters. In the linear elastic regime, stiffness terms scale linearly with the elastic modulus and inertial quantities scale linearly with the density; therefore, this choice isolates the effects of geometry, shell kinematics and discretization without loss of generality.

4.1. Thin-walled circular cylinder (pipe)

A thin-walled circular cylinder provides an analytical reference for axial, bending, torsional, and shear stiffness, as well as for mass and sectional inertia. Table 1 summarizes the geometry and material parameters.

Analytical reference properties follow the standard thin-walled theory for closed circular sections, using

$$A = \pi\left(\left(R+\frac{t}{2}\right)^2 - \left(R-\frac{t}{2}\right)^2\right) = 2\pi R\, t, \tag{15a}$$

$$I_y = I_z = \frac{\pi}{4}\left(\left(R+\frac{t}{2}\right)^4 - \left(R-\frac{t}{2}\right)^4\right) \approx \pi R^3 t, \tag{15b}$$

$$J = \frac{\pi}{2}\left(\left(R+\frac{t}{2}\right)^4 - \left(R-\frac{t}{2}\right)^4\right) \approx 2\pi R^3 t, \tag{15c}$$

$$G = \frac{E}{2(1+\nu)}. \tag{15d}$$

Fig. 2 illustrates the convergence of the extracted axial, bending, and torsional stiffness terms with increasing circumferential discretization for linear shells, where N_θ indicates the number of shell elements along the circumference of the pipe. Table 2 shows that, for the considered thickness ratio $t/R \ll 1$, these terms converge rapidly and match the analytical values closely for both linear and quadratic elements.

In the present circular-tube meshes, the mid-side nodes of the quadratic shell elements are not projected onto the true circumferential arc; they lie on the straight edges between corner nodes. As a result, both linear and quadratic meshes provide the same piecewise-linear geometric approximation of the circumference, so linear and quadratic elements lead to essentially identical geometric convergence.

Shear stiffness terms are discussed separately because their effective value depends on modeling assumptions (e.g., shear-deformation theory and shear correction). We therefore focus on convergence and on a comparison between shell kinematics, using a 3D solid discretization as a reference. Fig. 3 shows the extracted D_{22} versus the circumferential discretization N_θ: KL and RM shells provide practically indistinguishable values within the considered discretization range. Moreover, the shell-based results converge more rapidly and approach an asymptotic value that is consistent with the 3D reference. As shown in the next benchmark (plate with increasing thickness), this agreement is not general once out-of-plane shear stresses become non-negligible.

4.2. Inertial properties: Mass per unit length and sectional inertia

The extracted inertial properties are compared against analytical expressions for a thin-walled circular pipe.

Analytical reference. For material density ρ, the mass per unit length is

$$\mu = \rho A = \rho\, 2\pi R t. \tag{16}$$

Assuming a uniform pipe of length ℓ, the sectional inertia about the pipe axis and the transverse axes read

$$\begin{aligned} I_x &= \rho\, J_x \\ I_y &= \rho\, J_y \end{aligned} \tag{17}$$

with $I_z = I_y$ by symmetry.

Convergence. Fig. 4 shows the convergence of the extracted mass per unit length and sectional inertia versus the circumferential discretization N_θ. Both shell and solid models converge to the analytical values, with the shell discretizations achieving a given accuracy with fewer degrees of freedom in this benchmark.

4.3. Flat plate: Thickness effect on shear stiffness

To isolate the influence of shear deformation and thickness on the extracted section terms, a square flat plate of side length $b = 0.2$ m is analyzed at two representative thickness values, $t = 0.02$ m and $t = 0.1$ m, as summarized in Table 3. The two configurations are selected to

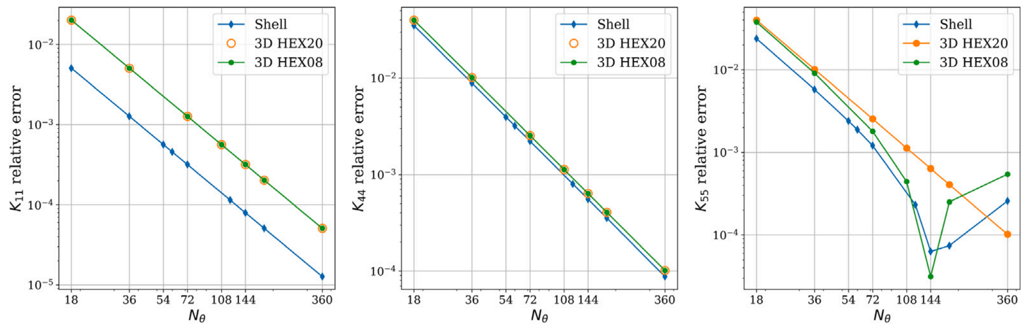

Fig. 2. Pipe benchmark: convergence of extracted stiffness terms using linear shell elements.

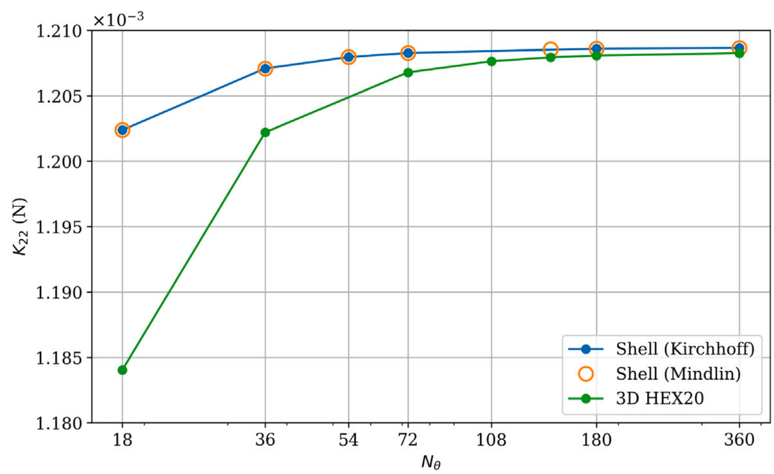

Fig. 3. Pipe: comparison of extracted shear stiffness (D_{22}) obtained with Kirchhoff–Love and Reissner–Mindlin shells, against a 3D reference discretization with one quadratic brick element through the thickness.

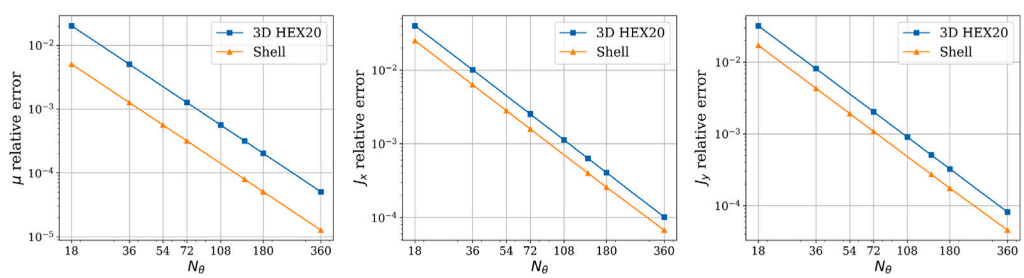

Fig. 4. Thin-walled pipe: convergence of extracted inertial properties (mass per unit length and sectional inertias) versus the number of elements N_θ along the circumference.

compare a lower-thickness case with a case in which shear-deformation effects become more pronounced. Fig. 5 summarizes the adopted reference axes and the discretization layout: axis 1 is aligned with the beam (axial) direction, axis 2 is normal to the plate mid-surface, i.e., it is the thickness direction, and axis 3 lies in the plate plane. The six investigated configurations (shell and 3D reference models, and their mesh parameters) are listed in Table 4.

For the thin plate ($t = 0.02$), KL and RM shells agree closely with the solid reference for the diagonal stiffness terms, with only a minor overestimation of D_{22}, the transverse shear stiffness, and D_{44}, the torsional stiffness, by the KL model (Table 5). For the thick plate ($t = 0.1$), the KL model substantially overestimates D_{22} and D_{44}, whereas the RM model remains consistent with the solid reference (3D) and the analytical estimates. The analytical shear- and torsion-related values reported in Tables 5 and 6 are derived from strain–energy definitions following Timoshenko [18]. In particular, the torsional stiffness is written as $D_{44} = GJ_t$, where J_t is the Saint-Venant torsion constant of the rectangular section, while the shear stiffness follows from the corresponding energy-equivalent shear correction. This behavior is consistent with the neglect of transverse shear deformation in KL kinematics and motivates the use of RM shells when shear contributions are not negligible [6].

Table 3
Flat plate benchmark: geometry, thickness range, and material parameters used to assess shear-deformation effects.

Parameter	Symbol	Value	Units
Side length	b	0.2	m
Thickness	t	$0.02 \to 0.1$	m
Young's modulus	E	1	N/m^2
Poisson's ratio	ν	0.3	–
Density	ρ	1	kg/m^3

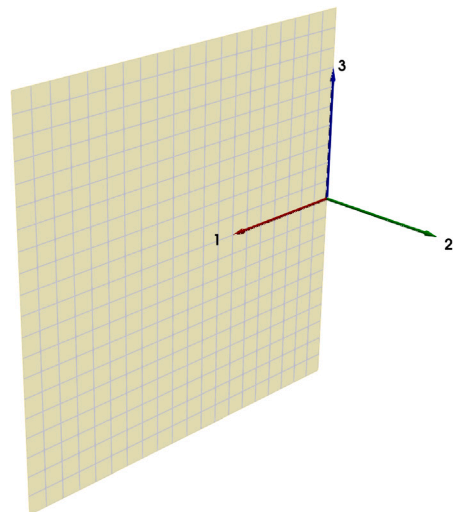

Fig. 5. Plate benchmark: shell discretization and reference axes (beam axis along 1).

Table 4
Flat plate benchmark: shell and solid reference discretizations for representative thin and thick configurations.

Case	t	model	discretization
1	0.02	KL	20×20
2	0.02	RM	20×20
3	0.02	HEX20	$20 \times 2 \times 20$
4	0.1	KL	20×20
5	0.1	RM	20×20
6	0.1	HEX20	$20 \times 10 \times 20$

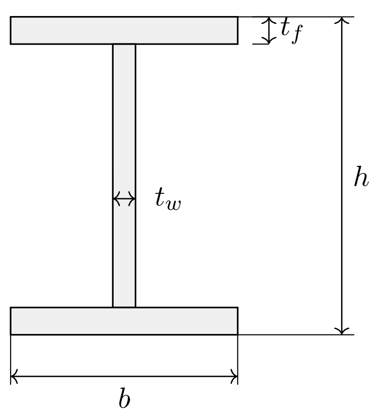

Fig. 6. IPE100 cross-section: Definition of geometric parameters.

4.4. Steel I-section (IPE100): Shell versus 3D benchmark

To complement the canonical benchmarks (pipe and plate) and before addressing laminated thin-walled sections, we analyze a steel I-section representative of engineering profiles. The geometry corresponds to an IPE100 section; the material is homogeneous isotropic steel. Shell-based section characterization (KL and RM) is compared against a three-dimensional reference model.

Geometry and material. Fig. 6 defines the adopted geometric parameters: total height h, flange width b, web thickness t_w, and flange thickness t_f. The corresponding values and material properties are summarized in Table 7.

Flange-web junction treatment and overlap mitigation. When an I-section is modeled using intersecting shell mid-surfaces with assigned thickness, a small geometric overlap may arise at the flange–web junction: both the flange and the web contribute thickness in the same region, effectively double-counting cross-sectional area and second moments of area. This mechanism is schematically illustrated in Fig. 7. As a result, axial and bending-dominated stiffness terms can be artificially increased.

To mitigate this effect, an overlap-free construction is adopted: the flange mid-surfaces are shifted outward by $\pm t_f/2$ (top/bottom flange, respectively) and the web height is reduced by t_f, so that the flange and web thickness regions meet without overlap. The stiffness comparison reported below is based on this overlap-free shell geometry.

Real hot-rolled IPE profiles also include rounded roots at the flange-web junction. The present IPE100 shell model intentionally adopts an idealized sharp-corner plate representation of the section. Such radii are naturally represented in a three-dimensional solid model. Within a reduced shell-based description, their effect could in principle be approximated by adding local beam-type correction elements at the junction, with sectional properties chosen to represent the material contribution of the rounded root not captured by the idealized plate assembly. This would lead to a mixed shell-beam model, which is compatible at the nodal level because both shell and beam elements carry translational and rotational degrees of freedom. However, such a correction would require a separate characterization and validation of the added beam sections, especially for shear- and torsion-related terms. Since the purpose of the present benchmark is to assess the shell-based characterization of a simplified thin-walled representation, and since artificial flange-web overlap can be removed directly by the offset construction described above, root-radius corrections are left as a possible extension.

A similar mixed shell-beam strategy may be more relevant for thin-walled structures with explicit longitudinal stiffeners or stringers, where the beam components provide a non-negligible stiffness and inertia contribution and are part of the intended structural idealization.

Comparison of extracted stiffness. Table 8 compares the diagonal stiffness terms obtained from shell models against the three-dimensional reference. After removing the junction overlap, D_{11} and D_{55} match the 3D reference essentially to numerical precision, confirming that the overlap-free construction provides results that match the 3D reference to numerical precision. The remaining differences are concentrated in shear-related terms (D_{22}, D_{33}) and in torsion (D_{44}), where the KL and RM shell formulations exhibit a small but noticeable divergence, while D_{66} remains only weakly affected, as expected.

For open thin-walled sections, the torsional term of a conventional six-degree-of-freedom beam model requires a specific interpretation. The coefficient reported here as D_{44} is the Saint-Venant torsional stiffness associated with the present reduction, corresponding to the energy contribution governed by the twist rate. Although the sectional warping field is represented within the finite element slice and condensed during the reduction, it is not retained as an independent generalized coordinate in the resulting six-degree-of-freedom beam model. Consequently, D_{44} does not include the Vlasov-type warping stiffness $D_\omega = EI_\omega$, which is associated with the derivative of the twist rate and with the corresponding bimoment [11]. It should therefore not be interpreted as the apparent torsional stiffness of a finite open-section member under arbitrary restrained-warping boundary conditions.

4.5. Laminated orthotropic box with classical-lamination-theory-based equivalent single-layer shells

Finally, the method is applied to a thin-walled rectangular box made of graphite/epoxy laminates, originally studied in several configurations in the literature [19–21]. The goal is to quantify the accuracy of CLT-based Equivalent Single-Layer (ESL) shell models when used within the section characterization framework, compared to ply-resolved three-dimensional laminate references.

Table 5
Flat plate (thin case): extracted diagonal stiffness terms D_{ii} for 3D, Kirchhoff–Love (KL) and Reissner–Mindlin (RM) models; highlighted KL values depart from 3D, RM, and analytical trends.

Term	Units	3D	KL	RM	Analytical
D_{11}	N	$4.000 \cdot 10^{-3}$	$4.000 \cdot 10^{-3}$	$4.000 \cdot 10^{-3}$	$4.000 \cdot 10^{-3}$
D_{22}	N	$2.757 \cdot 10^{-4}$	$2.894 \cdot 10^{-4}$	$2.712 \cdot 10^{-4}$	$2.767 \cdot 10^{-4}$
D_{33}	N	$1.282 \cdot 10^{-3}$	$1.286 \cdot 10^{-3}$	$1.286 \cdot 10^{-3}$	$1.282 \cdot 10^{-3}$
D_{44}	$\mathrm{N\,m^2}$	$1.923 \cdot 10^{-7}$	$2.051 \cdot 10^{-7}$	$1.935 \cdot 10^{-7}$	$1.922 \cdot 10^{-7}$
D_{55}	$\mathrm{N\,m^2}$	$1.333 \cdot 10^{-5}$	$1.333 \cdot 10^{-5}$	$1.333 \cdot 10^{-5}$	$1.333 \cdot 10^{-5}$
D_{66}	$\mathrm{N\,m^2}$	$1.333 \cdot 10^{-7}$	$1.333 \cdot 10^{-7}$	$1.333 \cdot 10^{-7}$	$1.333 \cdot 10^{-7}$

Table 6
Flat plate (thick case): extracted diagonal stiffness terms D_{ii} for 3D, Kirchhoff–Love (KL) and Reissner–Mindlin (RM) models; highlighted KL values depart from 3D, RM, and analytical trends.

Term	Units	3D	KL	RM	Analytical
D_{11}	N	$2.000 \cdot 10^{-2}$	$2.000 \cdot 10^{-2}$	$2.000 \cdot 10^{-2}$	$2.000 \cdot 10^{-2}$
D_{22}	N	$6.034 \cdot 10^{-3}$	$3.618 \cdot 10^{-2}$	$6.035 \cdot 10^{-3}$	$6.034 \cdot 10^{-3}$
D_{33}	N	$6.407 \cdot 10^{-3}$	$6.430 \cdot 10^{-3}$	$6.430 \cdot 10^{-3}$	$6.407 \cdot 10^{-3}$
D_{44}	$\mathrm{N\,m^2}$	$1.759 \cdot 10^{-5}$	$2.564 \cdot 10^{-5}$	$1.760 \cdot 10^{-5}$	$1.759 \cdot 10^{-5}$
D_{55}	$\mathrm{N\,m^2}$	$6.667 \cdot 10^{-5}$	$6.667 \cdot 10^{-5}$	$6.667 \cdot 10^{-5}$	$6.667 \cdot 10^{-5}$
D_{66}	$\mathrm{N\,m^2}$	$1.667 \cdot 10^{-5}$	$1.667 \cdot 10^{-5}$	$1.667 \cdot 10^{-5}$	$1.667 \cdot 10^{-5}$

Table 7
Geometry and material parameters for the IPE100 benchmark.

Quantity	Symbol	Value	Unit
Total height	h	100.0	mm
Flange width	b	55.0	mm
Web thickness	t_w	4.1	mm
Flange thickness	t_f	5.7	mm
Young's modulus	E	210	GPa
Poisson's ratio	ν	0.30	–
Density	ρ	7850	kg/m³

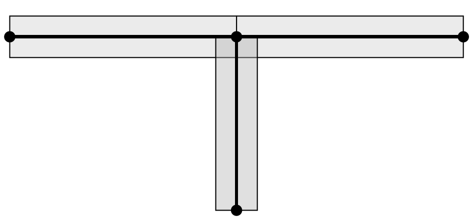

Fig. 7. Flange–web junction in shell mid-surface models: schematic overlap that can arise when intersecting mid-surfaces are assigned thickness. Offsetting the flange mid-surfaces by $\pm t_f/2$ and reducing the web height by t_f removes the overlap and improves agreement with the 3D reference (Table 8).

4.5.1. Geometry and laminate definition

The box outer dimensions are 24.21 mm × 13.64 mm with wall thickness 0.76 mm (see schematic in Fig. 8). Orthotropic ply properties are reported in Table 9, and six layups are defined in Table 10. The layup notation starts from the innermost ply and ends with the outermost ply; 0° fibers are aligned with the beam axis. Positive angles denote a right-hand rotation about the outward wall normal.

4.5.2. Classical lamination theory condensation for equivalent single layer shells

For each wall laminate, the ABD matrices are computed via classical lamination theory by integrating the ply stiffnesses through thickness and assembling extensional, coupling, and bending contributions [14, 22]. These laminate properties are then assigned to single-layer KL and RM shell models (ESL approach) and used within the same section-characterization pipeline as the three-dimensional references.

The six configurations are considered separately: three antisymmetric (cases 1–3) and three symmetric (cases 4–6) layups, as the two groups populate the stiffness matrix differently.

4.5.3. Comparison metrics and results: Antisymmetric layups (Cases 1–3)

For the antisymmetric layups (cases 1–3 in Table 10), only the diagonal stiffness terms $D_{11}, \dots, D_{66}$ and the couplings D_{14}, D_{25}, and D_{36} are expected to be non-zero. For each case, the shell-based stiffness matrices obtained with the KL and RM formulations are compared against the 3D solid reference. Since the matrices are symmetric to numerical precision, only the relevant upper-triangular entries are considered.

For a generic stiffness entry, the relative error of a shell model $(\cdot) \in \{\mathrm{KL}, \mathrm{RM}\}$ with respect to the 3D reference is defined as

$$\varepsilon_{ij}^{(\cdot)} = \frac{\left|D_{ij}^{(\cdot)} - D_{ij}^{(3D)}\right|}{\left|D_{ij}^{(3D)}\right|}. \tag{18}$$

In the present cases, all the considered reference terms satisfy $|D_{ij}^{(3D)}| \gtrsim 10^4$, so no denominator regularization is required.

Tables 11 and 12 report mean error values computed separately for diagonal and coupling terms. Specifically, $\bar{\varepsilon}_{\mathrm{diag}}$ denotes the mean relative error over the diagonal entries $D_{11}, \dots, D_{66}$, whereas $\bar{\varepsilon}_{\mathrm{cpl}}$ denotes the mean relative error over the coupling entries D_{14}, D_{25} and D_{36}. For completeness, the corresponding maximum-error summaries are reported in Appendix B.

Across all configurations, both KL and RM ESL shells accurately reproduce membrane- and bending-dominated stiffness trends; maximum diagonal relative errors remain typically on the order of 10^{-2}, and coupling discrepancies are of comparable or smaller magnitude.

4.5.4. Comparison metrics and results: Symmetric layups (Cases 4–6)

For the symmetric layups (cases 4–6 in Table 10), the extracted sectional stiffness matrix is symmetric and exhibits the expected block structure, with non-zero entries confined to the upper-left and lower-right 3 × 3 blocks. Accordingly, we consider the diagonal terms $D_{11}, \dots, D_{66}$ and the off-diagonal couplings within each block, i.e. $(1,2)$, $(1,3)$, $(2,3)$ and $(4,5)$, $(4,6)$, $(5,6)$. For each case, the KL and RM shell results are compared against the 3D solid reference.

For the diagonal terms, discrepancies are quantified through the standard relative error

$$\varepsilon_{ii}^{(\cdot)} = \frac{\left|D_{ii}^{(\cdot)} - D_{ii}^{(3D)}\right|}{\left|D_{ii}^{(3D)}\right|}, \qquad (\cdot) \in \{\mathrm{KL}, \mathrm{RM}\}. \tag{19}$$

Table 8
IPE100 benchmark: comparison of diagonal stiffness terms between 3D and shell models.

Term	Units	3D	RM	Err. RM [%]	KL	Err. KL [%]
D_{11}	N	$2.080 \cdot 10^8$	$2.080 \cdot 10^8$	0.000	$2.080 \cdot 10^8$	0.000
D_{22}	N	$4.302 \cdot 10^7$	$4.234 \cdot 10^7$	−1.574	$4.233 \cdot 10^7$	−1.607
D_{33}	N	$3.056 \cdot 10^7$	$3.002 \cdot 10^7$	−1.748	$3.090 \cdot 10^7$	1.117
D_{44}	N m^2	$7.031 \cdot 10^2$	$6.738 \cdot 10^2$	−4.168	$7.151 \cdot 10^2$	1.707
D_{55}	N m^2	$3.430 \cdot 10^5$	$3.430 \cdot 10^5$	0.001	$3.430 \cdot 10^5$	0.001
D_{66}	N m^2	$3.330 \cdot 10^4$	$3.331 \cdot 10^4$	0.022	$3.330 \cdot 10^4$	0.017

Errors are computed as $100\left(D_{ii}^{(\cdot)} - D_{ii}^{(3D)}\right)/D_{ii}^{(3D)}$ and retain the sign.

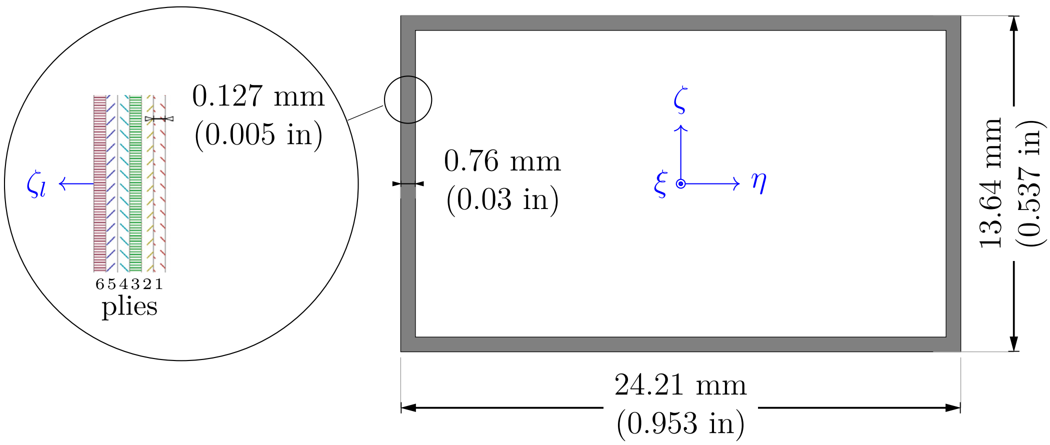

Fig. 8. Laminated orthotropic box: geometry and local reference axes.

Table 9
Orthotropic ply material properties used in the laminated box benchmark.

Quantity	Symbol	Value	Units
Longitudinal modulus	E_L	141.963	GPa
Transverse modulus	E_T	9.791	GPa
Shear modulus	G_{LT}	5.998	GPa
Poisson's ratio	ν_{LT}	0.42	–
Poisson's ratio	ν_{TN}	0.42	–

Table 10
Laminated box benchmark: layup definitions for each wall.

Case	Upper wall	Lower wall	Left wall	Right wall
1	$[15°]_6$	$[15°]_6$	$[15°]_6$	$[15°]_6$
2	$[0°, 30°]_3$	$[0°, 30°]_3$	$[0°, 30°]_3$	$[0°, 30°]_3$
3	$[0°, 45°]_3$	$[0°, 45°]_3$	$[0°, 45°]_3$	$[0°, 45°]_3$
4	$[15°]_6$	$[-15°]_6$	$[15°, -15°]_3$	$[-15°, 15°]_3$
5	$[30°]_6$	$[-30°]_6$	$[30°, -30°]_3$	$[-30°, 30°]_3$
6	$[45°]_6$	$[-45°]_6$	$[45°, -45°]_3$	$[-45°, 45°]_3$

Table 11
Antisymmetric layups: mean relative error of diagonal stiffness terms ($\bar{\epsilon}_{\text{diag}}$) for KL and RM models, with respect to the 3D reference.

Case	$\bar{\epsilon}_{\text{diag}}$	
	KL	RM
1	$1.168 \cdot 10^{-2}$	$1.171 \cdot 10^{-2}$
2	$7.622 \cdot 10^{-3}$	$8.083 \cdot 10^{-3}$
3	$9.437 \cdot 10^{-3}$	$9.986 \cdot 10^{-3}$

Table 12
Antisymmetric layups: mean relative error of coupling stiffness terms ($\bar{\epsilon}_{\text{cpl}}$) for KL and RM models, with respect to the 3D reference.

Case	$\bar{\epsilon}_{\text{cpl}}$	
	KL	RM
1	$1.877 \cdot 10^{-3}$	$1.890 \cdot 10^{-3}$
2	$1.172 \cdot 10^{-3}$	$2.383 \cdot 10^{-3}$
3	$2.319 \cdot 10^{-3}$	$2.558 \cdot 10^{-3}$

Table 13
Symmetric layups: mean relative error of diagonal stiffness terms ($\bar{\epsilon}_{\text{diag}}$) for KL and RM models, with respect to the 3D reference.

Case	$\bar{\epsilon}_{\text{diag}}$	
	KL	RM
4	$8.40 \cdot 10^{-3}$	$9.16 \cdot 10^{-3}$
5	$6.15 \cdot 10^{-3}$	$6.97 \cdot 10^{-3}$
6	$5.62 \cdot 10^{-3}$	$6.17 \cdot 10^{-3}$

For the off-diagonal couplings, the corresponding reference entries may be orders of magnitude smaller than the diagonal stiffnesses, so a relative error normalized by $|D_{ij}^{(3D)}|$ can become overly sensitive and yield inflated values that are not representative of the impact on the overall stiffness. We therefore report coupling discrepancies using a normalized absolute metric, scaled by the maximum diagonal stiffness of the corresponding block:

$$\eta_{ij}^{(\cdot)} = \frac{\left|D_{ij}^{(\cdot)} - D_{ij}^{(3D)}\right|}{D_b}, \qquad D_b = \max_{p\in b}\left|D_{pp}^{(3D)}\right|, \tag{20}$$

where $b = \{1, 2, 3\}$ for couplings in the upper-left block and $b = \{4, 5, 6\}$ for couplings in the lower-right block.

Tables 13 and 14 report mean error metrics computed over the diagonal terms ($\bar{\epsilon}_{\text{diag}}$) and over the in-block couplings ($\bar{\eta}_{\text{cpl}}$), respectively. The largest errors are reported in Appendix B.

Interestingly, KL and RM results are very close for both antisymmetric and symmetric layups in this benchmark: KL is marginally more accurate in most cases, but both stay within the same error order, suggesting that, for the present laminates and geometry, discrepancies are primarily driven by the CLT condensation and the intrinsic differences between 3D and ESL kinematics, rather than by transverse shear effects alone.

Table 14
Symmetric layups: mean normalized absolute error of coupling stiffness terms ($\overline{\eta}_{\mathrm{cpl}}$) for KL and RM models, with respect to the 3D reference.

Case	$\overline{\eta}_{\mathrm{cpl}}$	
	KL	RM
4	$1.58 \cdot 10^{-3}$	$1.57 \cdot 10^{-3}$
5	$2.25 \cdot 10^{-3}$	$2.21 \cdot 10^{-3}$
6	$1.65 \cdot 10^{-3}$	$1.61 \cdot 10^{-3}$

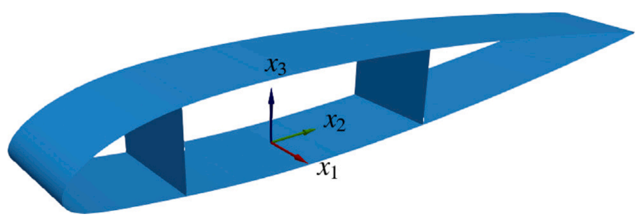

Fig. 9. Composite helicopter-blade section used as application case: NACA 23012 external skin, internal spar strips, and quarter-chord reference point.

Table 15
Composite helicopter-blade section: geometry and shell modeling assumptions.

Quantity	Symbol	Value	Unit/description
Airfoil profile	–	NACA 23012	–
Chord	c	72.5	mm
Maximum thickness	$t_{\max}$	8.70	mm
Reference point	–	$x/c = 0.25$	quarter chord
Skin laminate	–	[45°/45°]	CC90, two plies
Skin ply thickness	t_{CC90}	0.1	mm
Skin total thickness	t_{skin}	0.2	mm
Spar laminate	–	$[0°]_5$	HS300, five plies
Spar ply thickness	t_{HS300}	0.33	mm
Spar total thickness	t_{spar}	1.65	mm
First spar position from LE	$x_{2_{s1}}$	9.91	mm
Second spar position from LE	$x_{2_{s2}}$	36.48	mm
First spar position	$x_{2_{s1}}/c$	0.137	–
Second spar position	$x_{2_{s1}}/c$	0.503	–

4.6. Application to a composite helicopter-blade section

As a final application-oriented case, the proposed shell-based characterization procedure is applied to a composite helicopter-blade section inspired by the BeSaME wind-tunnel rotor blade model [23]. Unlike the previous benchmarks, this case is not intended as an additional validation against a three-dimensional reference model; rather, it demonstrates the direct use of the method on a realistic composite thin-walled section with closed skin geometry, anisotropic shell layups, and internal shell-modeled reinforcements.

The section is based on a NACA 23012 profile with chord $c = 72.5$ mm and maximum thickness 8.70 mm. The blade is untwisted in the considered configuration. The Rohacell foam core is omitted from the structural model, consistently with its role as a non-structural component used to preserve the blade geometry. The structural shell model therefore includes the external CC90 skin and the two internal HS300 spar strips. The origin of the section reference frame is placed at the quarter chord. The axis x_2 is oriented along the chord, positive from the leading edge to the trailing edge, and x_3 completes the right-handed triad, approximately along the airfoil thickness direction (see Fig. 9 and Table 15).

The CC90 skin is modeled using two plies oriented at 45° with respect to the blade longitudinal direction, a layup selected to resist torsional loads on the blade section. The HS300 spar strips are modeled as five unidirectional plies oriented at 0° with respect to the blade axis. The material properties used in the shell model are summarized in Table 16. The stiffness values are taken from the material data sheet, while the densities refer to the impregnated composite values used in the numerical model.

The extracted stiffness terms are reported in Table 17. The values are given in SI units and terms such that $|D_{ij}| < 10^{-4} \cdot \sqrt{D_{ii} D_{jj}}$ are omitted. The non-zero coupling terms reflect the combined effect of the airfoil geometry, the quarter-chord reference point, the anisotropic skin layup, and the chordwise placement of the spar strips.

The corresponding mass and sectional inertia properties per unit length are reported in Table 18, where μ is the mass per unit length, the transverse coordinates of the center of gravity $x_{i,cm}$ are reported with respect to the adopted quarter-chord section reference frame and the inertia components j_{ij} are expressed per unit length.

This application illustrates the use of the proposed extraction procedure on a realistic composite blade section composed of multiple shell components with different laminate properties. The example complements the previous controlled benchmarks by showing how the same workflow can be applied to a practical multi-component thin-walled section, including anisotropic skin layups and shell-modeled spar reinforcements.

5. Discussion

Starting from the interface reduction operator used for 3D solid discretizations and validated in [3], the shell extension requires primarily a kinematic adjustment: in addition to displacements, nodal rotations must be constrained consistently with the handle rotation to prevent spurious relative rotations at the section boundaries (Eq. (6)). Once this mapping is in place, the remainder of the extraction procedure introduced there (i.e. static condensation, identification of the mapping $\mathbf{X}$ from equilibrated generalized loads to condensed displacements, and energetic equivalence leading to the sectional compliance and stiffness matrices, $\mathbf{G}$ and $\mathbf{D}$) remains unchanged.

Across the benchmarks considered:

- **Pipe benchmark.** For a thin-walled closed section with $t/R \ll 1$, axial, bending, and torsional stiffness terms converge rapidly and are largely insensitive to KL vs RM choice and to linear vs quadratic interpolation. Shear stiffness terms converge more slowly, but for this circular closed section they remain nearly insensitive to the selected shell kinematics and converge toward the 3D reference.
- **Plate thickness study.** KL shells remain accurate in the lower-thickness configuration but can significantly overestimate shear-related stiffness terms when thickness increases. RM shells track solid references across the considered thickness range.
- **Steel I-section.** The IPE100 benchmark highlights a practical modeling issue specific to shell idealizations of built-up thin-walled sections: if intersecting mid-surfaces are assigned thickness without correction, flange–web overlap can artificially increase axial and bending-dominated stiffness terms. Once this overlap is removed by offsetting the flange mid-surfaces and reducing the web height accordingly, the axial and bending terms agree closely with the 3D reference, while the remaining differences are mainly associated with shear- and torsion-related terms.
- **Laminated orthotropic box.** CLT-based ESL shell models reproduce 3D reference stiffness trends well for membrane and bending contributions. KL and RM results are very close; typical maximum diagonal discrepancies are $\mathcal{O}(10^{-2})$, with coupling discrepancies of comparable or smaller order. These levels are often acceptable for beam-level analyses, especially when the reduced model provides substantially cheaper discretizations that can be leveraged for global model refinement.

Table 16
Composite helicopter-blade section: material properties used for the shell model.

Material	E_{11}/MPa	E_{22}/MPa	ν_{12}	ν_{21}	G_{12}/MPa	ρ/(kg//m^3)
HS300	117 000	200	0.28	0.025	4281	1680
CC90	56 345	56 345	0.0514	0.0514	4043	1530

Table 17
Composite helicopter-blade section: selected stiffness terms extracted from the shell model.

Term	Unit	Value
D_{11}	N	$3.445 \cdot 10^6$
D_{22}	N	$4.768 \cdot 10^5$
D_{33}	N	$9.202 \cdot 10^4$
D_{44}	N m^2	$5.661 \cdot 10^1$
D_{55}	N m^2	$2.425 \cdot 10^1$
D_{66}	N m^2	$1.221 \cdot 10^3$
D_{15}	N m	$3.529 \cdot 10^3$
D_{16}	N m	$3.951 \cdot 10^4$
D_{23}	N	$-7.984 \cdot 10^3$
D_{24}	N m	$-4.328 \cdot 10^2$
D_{34}	N m	$-1.242 \cdot 10^3$
D_{45}	N m^2	$1.782 \cdot 10^{-1}$
D_{56}	N m^2	$5.543 \cdot 10^1$

Table 18
Composite helicopter-blade section: extracted mass and inertial properties per unit length.

Quantity	Unit	Value
μ	kg m^{-1}	$8.734 \cdot 10^{-2}$
$x_{2,\mathrm{cm}}$	m	$-6.540 \cdot 10^{-3}$
$x_{3,\mathrm{cm}}$	m	$8.982 \cdot 10^{-4}$
j_{11}	kg m	$3.201 \cdot 10^{-5}$
j_{22}	kg m	$6.870 \cdot 10^{-7}$
j_{33}	kg m	$3.133 \cdot 10^{-5}$
j_{23}	kg m	$5.735 \cdot 10^{-7}$

- **Composite blade section.** The helicopter-blade application shows that the same extraction workflow can be applied to a realistic multi-component composite section, including a closed airfoil skin, anisotropic shell layups, and internal shell-modeled spar strips. This case illustrates the practical use of the method beyond controlled benchmarks, where the extracted stiffness and inertia properties can be used directly in beam-level models.

From a practical standpoint, these results suggest the following guidelines for thin-walled section characterization using shells:

i. KL shells are adequate when transverse shear contributions are negligible (very thin walls and membrane/bending dominated behavior);
ii. RM shells are preferable when shear-related stiffness terms or torsion-shear couplings are important, or when thickness is not extremely small;
iii. when shell mid-surfaces intersect, as in idealized I- or H-sections, thickness overlap should be checked and removed by a consistent offset or trimming strategy before interpreting axial and bending stiffness terms;
iv. for composite thin-walled laminates, the dominant source of approximation may lie in the CLT-based ESL condensation rather than the KL vs RM choice, and accuracy should be assessed relative to intended downstream quantities of interest;
v. application-oriented shell models can provide efficient sectional properties for complex thin-walled composite structures, but geometric details that are intentionally simplified in the shell representation should be assessed according to their expected influence on the quantities of interest.

A limitation of the present six-degree-of-freedom reduction concerns open thin-walled sections under non-uniform torsion or restrained-warping boundary conditions. In such cases, the overall torque-twist response may depend on the beam length, loading distribution, and warping constraints. The torsional coefficient identified by the present procedure should therefore be interpreted as the Saint-Venant torsional stiffness of the reduced beam model. The Vlasov warping stiffness and the associated bimoment are outside the scope of the current formulation and would require retaining an additional warping-related generalized coordinate, or adopting an equivalent higher-order torsional description [11].

6. Conclusions

A substructuring-based framework to extract beam sectional stiffness and inertia properties from short three-dimensional FE slices is extended to shell discretizations. The extension is achieved by redefining the rigid interface-handle mapping to include nodal rotations, yielding a kinematically consistent constraint for shell formulations while leaving the remainder of the extraction pipeline unchanged. Validation on a thin-walled pipe and a plate thickness sweep confirms the expected behavior of Kirchhoff–Love and Reissner–Mindlin shells: the first is accurate for thin, shear-negligible regimes, whereas the second is required to capture shear-related stiffness terms as thickness increases. Application to a laminated orthotropic box, with equivalent single-layer shell properties obtained from classical lamination theory, shows that both the Kirchhoff–Love and Reissner–Mindlin shell formulations accurately reproduce the stiffness trends of the three-dimensional solid reference model well, with typical maximum diagonal discrepancies on the order of 10^{-2} and comparable or smaller coupling discrepancies. The reduction to interface DOFs makes the cost independent of axial discretization after condensation. These results support the use of shell-based section characterization as a reliable and computationally efficient alternative to fully three-dimensional models for a wide range of thin-walled applications, provided that shell kinematics and laminate condensation are selected consistently with the desired level of accuracy.

CRediT authorship contribution statement

Claudio Caccia: Writing – original draft, Visualization, Validation, Software, Methodology, Data curation. **Marco Morandini:** Writing – review & editing, Methodology, Formal analysis, Conceptualization. **Pierangelo Masarati:** Writing – review & editing, Writing – original draft, Supervision, Methodology, Formal analysis, Conceptualization.

Declaration of generative AI and AI-assisted technologies in the manuscript preparation process

During the preparation of this work, the authors used OpenAI's ChatGPT for language editing, text refinement, and assistance in improving the clarity and organization of selected parts of the manuscript. The authors reviewed and edited the output as needed and take full responsibility for the content of the published article.

Declaration of competing interest

The authors declare that they have no known competing financial interests or personal relationships that could have appeared to influence the work reported in this paper.

Table B.19
Lay-up 1.

$6.630 \cdot 10^6$			$-1.314 \cdot 10^4$		
	$4.000 \cdot 10^5$			$6.401 \cdot 10^3$	
		$1.806 \cdot 10^5$			$6.863 \cdot 10^3$
			$5.474 \cdot 10^1$		
				$2.252 \cdot 10^2$	
sym.					$5.522 \cdot 10^2$

Table B.20
Lay-up 2.

$5.754 \cdot 10^6$			$-6.616 \cdot 10^3$		
	$4.384 \cdot 10^5$			$3.303 \cdot 10^3$	
		$1.915 \cdot 10^5$			$3.420 \cdot 10^3$
			$5.923 \cdot 10^1$		
				$2.008 \cdot 10^2$	
sym.					$4.814 \cdot 10^2$

Appendix A. Rigid-body inertia properties

This appendix reports compact expressions for the section mass per unit length, first moment, and sectional inertia tensor, obtained by matching the rigid-body kinetic energy of the condensed slice with that of an equivalent one-dimensional beam.

Following the rigid-section assumption for inertia, the condensed rigid-body inertia of the slice is computed as

$$\mathbf{M}_{\mathrm{rb}} = \mathbf{Z}_{\mathrm{rb}}^T \mathbf{M}_{BB} \mathbf{Z}_{\mathrm{rb}}, \tag{A.1}$$

where $\mathbf{M}_{BB}$ is the condensed interface mass, and $\mathbf{Z}_{\mathrm{rb}}$ maps the six rigid-body linear and angular velocity components at a reference end section to those of both end sections of the slice under a rigid-body motion assumption.

Equating $\mathbf{M}_{\mathrm{rb}}$ to the beam rigid-body inertia over length ℓ yields [24]:

$$m = \frac{1}{\ell}\mathbf{M}_{\mathrm{rb}}(1,1), \tag{A.2a}$$

$$\mathbf{S}_{\mathrm{refcm}} = -m\frac{\ell}{2}\mathbf{e}_1 - \frac{1}{\ell}\,\mathrm{ax}\left(\mathbf{M}_{\mathrm{rb}}(1{:}3,4{:}6)\right), \tag{A.2b}$$

$$\mathbf{J} = \frac{1}{\ell}\mathbf{M}_{\mathrm{rb}}(4{:}6,4{:}6) - m\frac{\ell^2}{3}\mathbf{e}_1\times^T\mathbf{e}_1\times + \frac{\ell}{2}\left(\mathbf{S}_{\mathrm{refcm}}\times^T\mathbf{e}_1\times + \mathbf{e}_1\times^T\mathbf{S}_{\mathrm{refcm}}\times\right),. \tag{A.2c}$$

where m is the mass per unit length, $\mathbf{S}_{\mathrm{ref}}$ is the static (or first-order inertia) moment per unit length with respect to the reference point in the section (the location of the center of mass is thus $\mathbf{p}_{\mathrm{cm}} = \mathbf{S}_{\mathrm{ref}}/m$), $\mathbf{J}$ is the inertia tensor per unit length with respect to the reference point of the section, $\mathbf{e}_1 = \{1; 0; 0\}$ is the unit vector aligned with the beam's axis, and $(\cdot)\times$ is the operator that transforms a vector $\mathbf{a}$ in a skew-symmetric matrix $\mathbf{a}\times$ such that the product $(\mathbf{a}\times)\mathbf{b}$ by another vector $\mathbf{b}$ yields the vector product between $\mathbf{a}$ and $\mathbf{b}$, $\mathbf{a}\times\mathbf{b}$, namely

$$\mathbf{a}\times = \begin{bmatrix} 0 & -a_3 & a_2 \\ a_3 & 0 & -a_1 \\ -a_2 & a_1 & 0 \end{bmatrix}. \tag{A.3}$$

Since the operator $(\cdot)\times$ yields a skew-symmetric matrix, $(\cdot)\times^T = -(\cdot)\times$. Finally, $\mathrm{ax}(\cdot)$ is the operator that extracts from a skew-symmetric matrix $(\cdot)\times$ the vector that generates it, namely $\mathrm{ax}(\mathbf{a}\times) = \mathbf{a}$.

Appendix B. Detailed laminate per-case tables

Here we report the complete stiffness matrices of the six configurations of the case described in Section 4.5, with all data presented in SI units (entries (1:3,1:3) in N, (1:3,4:6) in N m, and (4:6,4:6) in N m^2) (see Tables B.19–B.24).

Table B.21
Lay-up 3.

$4.721 \cdot 10^6$			$-2.680 \cdot 10^3$		
	$3.726 \cdot 10^5$			$1.343 \cdot 10^3$	
		$1.620 \cdot 10^5$			$1.385 \cdot 10^3$
			$5.015 \cdot 10^1$		
				$1.648 \cdot 10^2$	
sym.					$3.947 \cdot 10^2$

Table B.22
Lay-up 4.

$6.363 \cdot 10^6$	$8.389 \cdot 10^5$	$9.020 \cdot 10^1$			
	$3.995 \cdot 10^5$	$3.907 \cdot 10^1$			
		$1.846 \cdot 10^5$			
			$5.639 \cdot 10^1$	$-5.916 \cdot 10^1$	-1.076
				$2.022 \cdot 10^2$	$2.989 \cdot 10^{-1}$
sym.					$4.578 \cdot 10^2$

Table B.23
Lay-up 5.

$2.913 \cdot 10^6$	$7.077 \cdot 10^5$	$3.677 \cdot 10^2$			
	$5.475 \cdot 10^5$	$2.738 \cdot 10^2$			
		$3.192 \cdot 10^5$			
			$8.581 \cdot 10^1$	$-5.540 \cdot 10^1$	$-8.057 \cdot 10^{-1}$
				$9.507 \cdot 10^1$	$1.098 \cdot 10^{-1}$
sym.					$2.039 \cdot 10^2$

Table B.24
Lay-up 6.

$1.190 \cdot 10^6$	$2.972 \cdot 10^5$	$2.249 \cdot 10^2$			
	$4.218 \cdot 10^5$	$3.127 \cdot 10^2$			
		$3.243 \cdot 10^5$			
			$7.062 \cdot 10^1$	$-2.483 \cdot 10^1$	$-2.935 \cdot 10^{-1}$
				$4.096 \cdot 10^1$	$1.587 \cdot 10^{-2}$
sym.					$9.037 \cdot 10^1$

Data availability

Data will be made available on request.

References

[1] V. Giavotto, M. Borri, P. Mantegazza, G. Ghiringhelli, V. Carmaschi, G.C. Maffioli, F. Mussi, Anisotropic beam theory and applications, Comput. Struct. 16 (1983) 403–413, http://dx.doi.org/10.1016/0045-7949(83)90179-7.

[2] D.H. Hodges, Nonlinear composite beam theory, American Institute of Aeronautics and Astronautics, 2006, http://dx.doi.org/10.2514/4.866821.

[3] P. Masarati, C. Caccia, M. Morandini, Substructuring-based accurate beam section characterization from finite element analysis, Comput. Struct. 311 (2025a) 107720, http://dx.doi.org/10.1016/j.compstruc.2025.107720.

[4] T.J.R. Hughes, M. Cohen, M. Haroun, Reduced and selective integration techniques in the finite element analysis of plates, Nucl. Eng. Des. 46 (1978) 203–222, http://dx.doi.org/10.1016/0029-5493(78)90184-X.

[5] T. Belytschko, J.I. Lin, T. Chen-Shyh, Explicit algorithms for the nonlinear dynamics of shells, Comput. Methods Appl. Mech. Engrg. 42 (1984) 225–251, http://dx.doi.org/10.1016/0045-7825(84)90026-4.

[6] J.N. Reddy, Mechanics of Laminated Composite Plates and Shells: Theory and Analysis, CRC Press, 2003, http://dx.doi.org/10.1201/b12409.

[7] O.A. Bauchau, A beam theory for anisotropic materials, J. Appl. Mech. 52 (1985) 416–422, http://dx.doi.org/10.1115/1.3169063.

[8] N. Silvestre, D. Camotim, Second-order generalised beam theory for arbitrary orthotropic materials, Thin-Walled Struct. 40 (2002) 791–820, http://dx.doi.org/10.1016/S0263-8231(02)00026-5.

[9] P.B. Dinis, D. Camotim, N. Silvestre, GBT formulation to analyse the buckling behaviour of thin-walled members with arbitrarily branched open cross-sections, Thin-Walled Struct. 44 (2006) 20–38, http://dx.doi.org/10.1016/j.tws.2005.09.005.

[10] D. Camotim, C. Basaglia, N. Silvestre, GBT buckling analysis of thin-walled steel frames: a state-of-the-art report, Thin-Walled Struct. 48 (2010) 726–743, http://dx.doi.org/10.1016/j.tws.2009.12.003.

[11] C. Mittelstedt, Generalized beam theory for the analysis of thin-walled structures: a state-of-the-art survey, Thin-Walled Struct. 200 (2024) 111849, http://dx.doi.org/10.1016/j.tws.2024.111849.
[12] R. Bebiano, D. Camotim, R. Gonçalves, GBTUL 2.0: a second-generation code for the GBT-based buckling and vibration analysis of thin-walled members, Thin-Walled Struct. 124 (2018) 235–257, http://dx.doi.org/10.1016/j.tws.2017.12.002.
[13] S. Ádány, Buckling analysis of cold-formed steel members using CUFSM: conventional and constrained finite strip methods, in: CCFSS Proceedings of International Specialty Conference on Cold-Formed Steel Structures (1971–2018), 2006.
[14] R.M. Jones, Mechanics of Composite Materials, second ed., CRC Press, Boca Raton, 2018, http://dx.doi.org/10.1201/9781498711067.
[15] T.J.R. Hughes, R.L. Taylor, W. Kanoknukulchai, A simple and efficient finite element for plate bending, Internat. J. Numer. Methods Engrg. 11 (1977) 1529–1543, http://dx.doi.org/10.1002/nme.1620111005.
[16] E.N. Dvorkin, Nonlinear analysis of shells using the MITC formulation, Arch. Comput. Methods Eng. 2 (1995) 1–50, http://dx.doi.org/10.1007/BF02904994.
[17] R.J. Guyan, Reduction of stiffness and mass matrices, AIAA J. 3 (1965) 380, http://dx.doi.org/10.2514/3.2874.
[18] S.P. Timoshenko, J.N. Goodier, Theory of Elasticity, second ed., McGraw Hill, New York, 1951.
[19] M. Borri, G.L. Ghiringhelli, T. Merlini, Linear analysis of naturally curved and twisted anisotropic beams, Compos. Eng. 2 (1992) 433–456, http://dx.doi.org/10.1016/0961-9526(92)90036-6.
[20] S. Han, O.A. Bauchau, Nonlinear three-dimensional beam theory for flexible multibody dynamics, Multibody Syst. Dyn. 34 (2015) 211–242, http://dx.doi.org/10.1007/s11044-014-9433-8.
[21] W. Yu, D.H. Hodges, J.C. Ho, Variational asymptotic beam sectional analysis: an updated version, Internat. J. Engrg. Sci. 59 (2012) 40–64, http://dx.doi.org/10.1016/j.ijengsci.2012.03.006.
[22] S.W. Tsai, Introduction to Composite Materials, Routledge, 2018, http://dx.doi.org/10.1201/9780203750148.
[23] P. Masarati, E. Casciaro, A. Cocco, R. Sutov, P. Bettini, A. Zanotti, G. Bernardini, F. Liguori, J. Serafini, C. Pasquali, From strain measurements to rotor blade shape and loads reconstruction: the BeSaME project, in: CEAS/AIDAA 2025, Turin, Italy, 2025b.
[24] S. Han, O.A. Bauchau, Nonlinear, three-dimensional beam theory for dynamic analysis, Multibody Syst. Dyn. 41 (2017) 173–200, http://dx.doi.org/10.1007/s11044-016-9554-3.